Chemical Synthesis

Research Article

Copper-doped TiO₂ photocatalyst for advanced oxidation processes: reactive oxygen species generation mechanisms

Naizhen Yu[1,2], Collins Nganou[2], Dongchang Yang[2], Andrew Carrier[2], Ken Oakes[3], Mita Dasog[1,*] ID, Xu Zhang[2,*]

[1]Department of Chemistry, Dalhousie University, Halifax B3H 4R2, Nova Scotia, Canada.
[2]Department of Chemistry, Cape Breton University, Sydney B1P 6L2, Nova Scotia, Canada.
[3]Department of Biology, Cape Breton University, Sydney B1P 6L2, Nova Scotia, Canada.

*Correspondence to:** Prof. Mita Dasog, Department of Chemistry, Dalhousie University, 6299 South St., Halifax B3H 4R2, Nova Scotia, Canada. E-mail: mita.dasog@dal.ca; Prof. Xu Zhang, Department of Chemistry, Cape Breton University, 1250 Grand Lake Rd., Sydney B1P 6L2, Nova Scotia, Canada. E-mail: xu_zhang@cbu.ca

Abstract

Copper-doped anatase TiO₂ (Cu/TiO₂) has attracted significant attention in various sustainable chemical processes, including water splitting, carbon monoxide oxidation, carbon dioxide reduction, chemical synthesis, and advanced oxidation processes for water treatment. Reactive oxygen species (ROS) are involved in these processes, but a mechanistic understanding of ROS generation on Cu/TiO₂ surfaces has not been established. Combining experimental investigation and computational simulation, this work provides unequivocal evidence for superoxide radical anion ($O_2^{\cdot-}$) formation via reduction of the adsorbed oxygen by Cu^+ and hydroxyl radical ($^{\cdot}OH$) production by oxidation of lattice oxygen within the bridging Cu-O-Ti structure on Cu/TiO₂ surfaces. Under visible light irradiation, the ROS generation rates of Cu/TiO₂ are 7.2 times higher for $O_2^{\cdot-}$ and 11.2 times higher for $^{\cdot}OH$ than those of undoped TiO₂. The superior performance of Cu/TiO₂ has been demonstrated through its organic dye degradation, bactericidal activity, and biofilm disruption, indicating its wide applicability in water treatment and disinfection. The results and the methodologies will benefit the wide field of heterogeneous redox chemistry.

Keywords: Heterogeneous redox chemistry, sustainable chemistry, organic dye, biofilm, disinfectant, antimicrobial effect

INTRODUCTION

Reactive oxygen species (ROS), such as hydroxyl radicals (•OH) and superoxide radical anions ($O_2^{•-}$), are of prime importance in advanced oxidation processes for water treatment. Titanium dioxide (TiO_2), a heterogeneous photocatalyst, has been a research focus for decades because of its ability to absorb sunlight, efficient photon-to-current conversion, high chemical stability, and low toxicity[1]. However, pristine anatase has a large optical band gap (~3.2 eV) that restricts photon absorption to the ultraviolet (UV) range, which comprises only ~5% of the solar spectrum, thus limiting its energy conversion efficiency. Photocatalytic materials activated solely by visible light are particularly valuable, especially when paired with energy-efficient and cost-effective visible light-emitting diodes (LEDs)[2]. These LEDs are compact, affordable, environmentally friendly, and suitable for indoor use or scenarios where sunlight is unavailable. To enhance its absorption in the visible region, researchers have narrowed its band gap via dye sensitization[3], doping[4,5], defect engineering[6,7], and by fabricating composite materials[8-10].

Nanostructured photocatalysts based on transition metal-doped TiO_2 have enabled the development of efficient and sustainable photocatalysts for environmental, chemical, and energy applications[11,12], such as water splitting[13,14], hydrogen generation[15-17], carbon monoxide oxidation[17,18], carbon dioxide reduction[19-21], hydrogen activation[22-24], organic synthesis[25,26], and the water-gas shift reaction[27-29], among others. Catalysis using doped semiconductors is at the interface between homogeneous and heterogeneous catalysis in that they have discrete active sites that confer selective reactivity[30]; meanwhile, the semiconductor support also provides photocatalytic properties and the benefits of heterogeneous systems such as partitioning and filterability. Many insights regarding the structure-reactivity relationships of metal-doped TiO_2 have been discerned[16,18,31,32]; however, little research has investigated the atomic mechanisms that govern ROS generation in water and their impact on water treatment practices, such as the degradation of organic pollutants and disruption of bacteria and biofilms.

To fill this gap, this work documents the first mechanistic study of ROS production on the surface of copper-doped anatase (Cu/TiO_2). First, the experimental data unambiguously showed that the surface Cu atoms are the oxygen reduction sites for $O_2^{•-}$ production and the bridging Cu-O-Ti structures are the active centers for •OH generation. Second, the surface-dispersed Cu atoms accelerate ROS generation by increasing oxygen adsorption and surface hydrophilicity. Third, the Cu-doping modifies the electronic structure of anatase, narrows its band gap, improves charge separation, and facilitates charge migration by reducing the internal and charge transfer resistances (CTR). Finally, its promise for water treatment was demonstrated with high bactericidal, biofilm disruption, and organic dye degradation efficiencies. These discoveries not only establish Cu/TiO_2 as an excellent photocatalyst but also enhance the fundamental understanding of transition metal-doped TiO_2 catalysts in general, which may broaden their applicability in practice.

EXPERIMENTAL

Chemicals and materials

Titanium isopropoxide (97%), cupric acetate monohydrate [$Cu(OAc)_2 \cdot H_2O$, 98%], Rhodamine B (RhB) (95%), 1,4-benzoquinone (BQ, 98%), sodium azide (99.5%), ammonium oxalate monohydrate (99.5%), 5,5-dimethyl-1-pyrroline N-oxide (DMPO, 99%), organic solvents (≥ 99%) (*n*-pentane, *n*-hexane, *n*-heptane, *n*-octane, and *n*-decane), coumarin (98%), and 2,3-bis(2-methoxy-4-nitro-5-sulfophenyl)-2*H*-tetrazolium-5-carboxanilide (XTT sodium salt, 90%) were purchased from Sigma Aldrich (Oakville, ON, Canada). Isopropanol (99%), anhydrous ethanol, and hydrochloric acid (37%) were purchased from Thermo Fisher Scientific (Waltham, MA, USA). Methanol (95%) was purchased from VWR International Ltd. (Radnor, PA, USA). Type 1 water (18.2 MΩ·cm) was obtained from a Millipore Simplicity Water Purification System

(EMD Millipore, Burlington, MA, USA). All reagents were of analytical grade and were used as received without further purification.

Analytical and characterization methods

The surface hydrophilicities of the Cu/TiO_2 and undoped TiO_2 nanoparticles (NPs) were evaluated using the maximum particle dispersion (MPD) method[33]. Probing liquids were composed of aqueous ethanol in various ratios to form five binary mixtures ranging in surface tension from 22 mJ/m^2 (for pure ethanol) to 72 mJ/m^2 (for pure water). The NP sample (2 mg) was added to the series of probing liquids, each at 0.5 mL, vortexed for 1 min, and left undisturbed for 1 h to allow for natural sedimentation. After sedimentation, 200 μL of the supernatant from each probing liquid was carefully transferred from the centrifuge tubes to a 96-well microplate. Optical densities (OD = 400 nm) of these supernatants were measured using a microplate reader. Each measurement was performed in triplicate and the results were reported as mean ± standard deviation.

Powder X-ray diffraction (XRD) measurements measured the crystalline structure and phase. The measurements were performed using a Rigaku Ultima IV X-ray diffractometer (Rigaku, Tokyo, Japan) with Cu Kα radiation (λ = 1.54 Å) and a diffracted beam monochromator using a step scan mode with a step of 0.05° (2θ) and 3 counts/s per step. The samples were placed on a zero-background Si wafer. Anatase TiO_2 powder diffraction patterns were compared with reference to the International Center for Diffraction Data (ICDD) database[34,35].

The micromorphological structures were investigated by transmission electron microscopy (TEM) using a Hitachi HT7700 (Hitachi, Tokyo, Japan) at an operating voltage of 80-120 kV. The samples were dispersed in ethanol and sonicated for 20 min. The dispersion was then drop-cast onto carbon-coated Ni TEM grids for analysis. The particle size distribution was obtained by measuring the individual diameters of ~100 particles from representative TEM images. The high-angle annular dark-field (HAADF) images in scanning TEM (STEM) mode were recorded using a Thermo Fisher Scientific Talos 200X (Waltham, MA, USA) at an operating voltage of 200 kV with a spot size of < 1 nm, and the convergence semi-angle of 10.5 mrad for analyzing Cu distribution information. The particles were drop-cast onto a Ni grid to avoid contamination from Cu grids typically used in electron microscopy experiments.

The X-ray photoelectron spectra (XPS) were measured using a Thermo VG Scientific Multilab 2000 spectrometer (Waltham, MA, USA), and high-resolution spectra were recorded with a pass energy of 30 eV and a step size of 0.1 eV. The spectra were fitted using CasaXPS software. All binding energies were referenced to the C 1s peak at 284.8 eV of the surface adventitious carbon.

UV-visible diffuse reflectance spectra (UV-Vis DRS) were measured by a SILVER-Nova spectrophotometer (StellarNet, Tampa, FL, USA) with a diffuse reflectance accessory over the range of 300-1,000 nm. The optical band gap energy was evaluated from the absorbance spectra through a Tauc plot, i.e., $[F(R\alpha) \times h\nu]^{1/2}$ against hν, where hν is the energy of the incident photon and $F(R\alpha)$ is the reflection in the Kubelka–Munk function[36]. The linear part of the curve was extrapolated to zero reflectance and the band gap energy was derived.

Surface charges of the Cu/TiO_2 NPs under various pH (pH 3, 5, 7, 9, and 11) were measured in triplicate using a Litesizer^{TM} 500 Particle Analyzer (Anton Paar, Graz, Austria) using dynamic light scattering (DLS). The dry powder form of Cu/TiO_2 was suspended in deionized water at a concentration of 50 μg/mL and then sonicated in a bath sonicator for 4 h to form a homogeneous dispersion before Zeta potential

measurements were performed at room temperature.

Electrochemical experiments

The transient photocurrent measurements, electrochemical impedance spectroscopy (EIS) measurements, and Mott–Schottky experiments were performed on a Corrtest CS2150 bipotentiostat electrochemical workstation (Wuhan, China) in a three-electrode cell with an applied potential of +0.6 V. NP-coated fluorine-doped tin oxide (FTO) served as the working electrode. Ag/AgCl and Pt mesh served as the reference and counter electrodes, respectively, and aqueous Na_2SO_4 (0.5 M) was used as the electrolyte solution. The photocurrent responses of the NPs were measured under 100 mW·cm^{-2} LED (400-800 nm, Dongguan, China) illumination intensity to simulate one sun. The light intensity of all experiments was consistent and measured using a PM100USB power detector (Thorlabs Inc., Newton, NJ, USA) with a standard photodiode sensor. Following the protocol suggested by the manufacturer, the FTO substrates were washed sequentially with toluene, methanol, acetone, ethanol, and distilled water using ultrasonication for 20 min in each solvent. Subsequently, to prepare the working electrode, 15 mg of the as-synthesized NPs were suspended in 20 μL of Nafion solution (5 wt%) and 0.5 mL of ethanol[37]. The obtained mixture was ground to form a slurry, which was then evenly spread as a thin film onto an FTO glass substrate with an active area of 1.0 cm^2 by drop casting. The coated FTO working electrode was then dried at room temperature. EIS was performed in the dark and under illumination in the frequency range of 0.1 Hz to 10 kHz with an applied potential of +0.6 V *vs.* standard hydrogen electrode (SHE). The flat band potential (E_{FB}) was determined using[38]

$$\frac{1}{C^2} = \frac{2}{A^2 \varepsilon_0 \varepsilon_r e N_D}\left(E - E_{FB} - \frac{k_B T}{e}\right)$$ (1)

where C is the interfacial capacitance, A is the interfacial area, ε_0 is the permittivity in vacuum, ε_r is the relative permittivity, N_D is the donor density, E is the externally applied potential, and T is the absolute temperature, e corresponds to the electronic charge, and k_B is the Boltzmann constant. Consequently, a plot of $1/C^2$ versus applied potential (E) will produce a line, which, when extrapolated to the x-axis, will indicate the flat-band potential of the semiconductor[37]. Potentials were referenced to the reversible hydrogen electrode (RHE) using the Nernst equation[39]:

$$E_{RHE} = E^0_{Ag/AgCl} + E_{Ag/AgCl} + 0.059 pH$$ (2)

Where $E^0_{Ag/AgCl}$ is 0.1976 V at 25 °C, and $E_{Ag/AgCl}$ is the measured potential *vs.* Ag/AgCl reference electrode.

Furthermore, the conduction band (CB) and valence band (VB) edge positions of a semiconductor were determined using[40,41]

$$E_{CB} = E_{FB} + k_B T_1 \times \ln\frac{N_{SC}}{N_{CB}}$$ (3)

$$E_{VB} = E_{CB} - E_g$$ (4)

where E_{CB} represents the CB edge, E_g is the band gap energy, E_{VB} represents the VB edge, T_1 is the semiconductor temperature (298 K), N_{sc} is the donor density (cm^{-1}), and N_{CB} is the effective density of states in the CB (7.8×10^{20} cm^{-3})[42].

Photocatalytic degradation experiment

RhB photodegradation in water was monitored to evaluate the photocatalytic performance of Cu/TiO$_2$ and undoped TiO$_2$ NPs. The mixture, including RhB (0.005 mg/mL, 20 mL) and TiO$_2$ NPs (20 mg), was irradiated with a 100 W LED visible light source. A wavelength filter of ≥ 400 nm was employed in all the photodegradation experiments to remove any UV light from the irradiation unless noted otherwise. The mixture was stirred at 400 rpm for 30 min in the dark to reach the adsorption equilibrium. The initial concentration of RhB was measured before the adsorption process, which was used to identify the dye adsorption ability of the NPs. The total irradiation time was 120 min, and the experiments were performed at room temperature. At regular 20-min intervals, 0.4 mL of the reaction mixture was taken, and the supernatant was isolated by centrifuging at 3,900 rpm for 10 min. The visible light absorbance of the supernatants was analyzed by the absorbance program of a FLUOstar Omega microplate reader (BMG Labtech, Cary, NC, USA). Unless stated otherwise, all RhB dye absorbance measurements were performed in a 96-well Corning™ plate (Corning, NY, USA). All photodegradation experiments were performed in triplicate with high reproducibility [relative standard deviation (RSD) < 1%]. Blank groups were performed in the absence of the catalysts under light irradiation. To test the effect of pH on RhB degradation, the pH of the samples was modified by drop-wise introduction of HCl (0.1 M) and NaOH (0.1 M) solutions to pH 3, 5, 7, 9, and 11, before performing the photodegradation and visible light absorbance measurement.

Identification and quantification of ROS

Scavenger test

The detailed ROS formation pathway of the photocatalytic dye degradation under neutral conditions was elucidated through the use of different selective scavengers that target h$^+$, O$_2^{\bullet-}$, $^{\bullet}$OH, and ^{1}O$_2$. The scavengers were added to photodegradation experiments where the final Cu/TiO$_2$ NP concentration was 1 mg/mL. The RhB photodegradation rate will decrease in the presence of specific scavengers that are responsible for its degradation under the reaction conditions. h$^+$, O$_2^{\bullet-}$, $^{\bullet}$OH, and ^{1}O$_2$ were scavenged by ammonium oxalate (AO, 10 mM), BQ (0.1 mM), methanol (200 mM), and sodium azide (200 mM), respectively[43-45].

Probe test

For the probe test to assess the ROS generation efficiency, two separate experiments were conducted using different probes for $^{\bullet}$OH and O$_2^{\bullet-}$, respectively. For $^{\bullet}$OH detection, a suspension was prepared by sonicating 20 mg of Cu/TiO$_2$ NPs in deionized water for 20 min. Coumarin was then added to this suspension in the dark and stirred at 400 rpm for 30 min to achieve adsorption equilibrium before dilution to a final volume of 20 mL with a final coumarin concentration of 100 μM. The prepared solution was irradiated under a 100 W LED equipped with a UV cut-off filter (λ > 400 nm), matching the light conditions of the photodegradation experiment. The light intensity was set at 100 mW/cm^2, with a total irradiation time of 120 min at room temperature. Aliquots (0.4 mL) were removed at 20-min intervals, and the supernatant was isolated by centrifuging at 3,900 rpm for 10 min. The fluorescence intensities of the supernatants were measured using the fluorescence program of a FLUOstar Omega Microplate Reader at excitation and emission wavelengths of 325 and 452 nm, respectively. The efficiency of $^{\bullet}$OH formation was calculated using

$$\eta_{\bullet OH} = \frac{I_t}{I_0} \tag{5}$$

where I_t represents the fluorescence intensity of the probe (coumarin) after irradiation at a given time t, I_0 denotes the initial fluorescence intensity of coumarin before irradiation, and $\eta_{\bullet OH}$ indicates the $^{\bullet}$OH generation efficiency.

For detecting $O_2^{\cdot-}$, a similar procedure using a final concentration of XTT of 2 mM was used and the absorbance of the product was recorded at 473 nm using the absorbance program of the FLUOstar Omega Microplate Reader. The efficiency of superoxide ion formation was determined using

$$\eta_{O_2^{\cdot-}} = \frac{A_t}{A_0} \tag{6}$$

Similarly, A_t represents the light absorbance of the probe (XTT) after irradiation over the time interval t, A_0 denotes its initial absorbance, and $\eta_{O_2^{\cdot-}}$ indicates the $O_2^{\cdot-}$ generation efficiency.

To determine the ROS formation efficiency under irradiation by various light sources, the probe experiment was repeated using distinct cut-off filters at 400, 420, 450, and 500 nm (Foric Optical Factory, Nantong, China). These filters were used to selectively remove wavelengths shorter than the specified cut-offs from the LED light source, allowing for the assessment of ROS production efficiency at or above 400, 420, 450, and 500 nm. For anaerobic experiments, the RhB-Cu/TiO$_2$ NP dispersions were sparged by nitrogen (80 mL/min) for 30 min while stirring before proceeding with photodegradation. $O_2^{\cdot-}$ and $^{\cdot}OH$ formation under anaerobic conditions was also tracked using their selective reactions with XTT (200 mM) and coumarin (1 mM), respectively.

EPR experiment
To further confirm $^{\cdot}OH$ formation, the Cu/TiO$_2$ NPs (5 mg) were sonicated in deionized water for 20 min to give a suspension. Subsequently, 20 μL of DMPO was added and shaken for a few seconds. In the final mixture, the NP and DMPO concentrations remained at 1 mg/mL and 20 mM, respectively. The mixture was quickly added to a capillary tube and was irradiated *in situ* with 100 W LED light for 30 s, before recording their electron paramagnetic resonance (EPR) spectra at 273 K. To identify $O_2^{\cdot-}$, the experiments were carried out similarly to that for $^{\cdot}OH$ detection; the only difference is using methanol as the solvent (not water, methanol quenches $^{\cdot}OH$ radicals). The EPR experiments were conducted using a SPINSCAN X spectrometer (Linev Systems, Conroe, TX, USA) operating at 9.200-9.500 GHz with a 100 kHz modulation frequency. The EPR parameters were as follows: field sweep, 15.0 mT; microwave frequency, 9.406 GHz; modulation amplitude, 100 uT; time constant, 0.046 s; and center field, 336.00 mT.

Antibacterial experiments
Bactericidal efficacy
E. coli strains were used to test the bactericidal effect of Cu/TiO$_2$. Before the antibacterial experiment, *E. coli* was aerobically incubated at 37 ± 0.1 °C for 24 h in Luria–Bertani (LB) broth and then harvested by centrifugation at 3,500 rpm for 5 min before resuspending in saline solution (0.85%, pH = 7) for rinsing. After another 5-min centrifugation, *E. coli* was resuspended in a fresh saline solution. The turbidity of the *E. coli* cell suspensions was measured at 600 nm using a FLUOstar Omega Microplate Reader and its concentration was adjusted to OD 600 = 0.1, which corresponded to approximately 8×10^7 colony-forming units per milliliter (CFU/mL). The adjusted *E. coli* was prepared for antibacterial and antibiofilm assays.

In the antibacterial experiment, a 200 mL Pyrex® crystallizing dish was used as the reaction vessel. First, 197.5 mL of sterilized saline (0.85%, pH = 7) was added to the dish. Then, NPs (200 mg) and 2.5 mL of the *E. coli* solution were added to the dish successively. The final concentrations of the NPs and microorganisms were 1 mg/mL and 1×10^6 CFU/mL, respectively. The mixture was placed on a magnetic stirrer to keep the NPs well dispersed during the experiment. The total irradiation time was 180 min. The mixture was irradiated with a 100 W LED lamp equipped with a UV cut-off filter (λ > 400 nm) with a light intensity of 100 mW·cm^{-2}. The experiments were performed at room temperature and neutral pH. The

solution temperature was maintained between 25-28 °C. During the experiment, sample aliquots (30 μL) were collected at 20-min intervals and spread uniformly on TS agar plates. Finally, the plates were incubated at 37 °C for 24 h before counting the *E. coli* colonies on each plate. The existence of bacteria was calculated using Chick's model, following

$$\eta = \log N_0 - \log N_t = -\log(\frac{N_t}{N_0}) \tag{7}$$

where η is the antibacterial efficiency, t is the irradiation time, N_0 represents the initial number of colonies, and N_t represents the number of *E. coli* at each time interval.

Antibiofilm assay
A crystal violet (CV) assay was used to evaluate biofilm disruption of Cu/TiO$_2$. First, to grow the biofilm, fully grown *E. coli* was diluted in fresh LB broth, and the bacteria concentration was adjusted to an optical density (OD) ~0.1 at 600 nm. Next, 2 mL of diluted culture was added to a 48-well cell culture plate (Corning Costar) and incubated for 48 h at 37 °C without shaking to allow for biofilm formation. Bacterial growth was indicated by measuring absorbance at OD 600. After incubation, the biofilm was rinsed with 85% saline solution three times to remove planktonic bacteria. Subsequently, the biofilm was treated with 1 mg/mL Cu/TiO$_2$ and TiO$_2$ NPs under LED irradiation followed by additional washing with saline, then incubated with 2 mL methanol for 30 min. The biofilms without Cu/TiO$_2$ treatment acted as controls. After incubation, biofilms in each well were stained with CV dye for 30 min at room temperature. To remove unbonded dye, the wells were gently rinsed three times with distilled water. Then, 2 mL of methanol was added to each well and allowed to act for ≥ 30 min for treating biofilm. After air-drying of the biofilm, CV was released in 200 μL of aqueous solution of acetic acid (33% V/V). Finally, the absorbance at 585 nm was measured using a FLUOstar Omega microplate reader and compared with positive and negative controls. To observe biofilm disruption using optical microscopy, sterile glass coverslips (0.6 cm × 0.6 cm) were placed in each well of the 48-well tissue culture plates during biofilm formation. After CV staining, the coverslips were gently removed from each well and air-dried at room temperature. The biofilms were visualized under a light microscope, and images were captured at 40× magnification.

Computational simulation
The anatase TiO$_2$ unit cell was designed using Crystal Maker X and one Ti atom was substituted with Cu to model Cu/TiO$_2$. Water and oxygen models were added to the system to model the oxygen adsorption process in water. The system was minimized by using the conjugate gradient method over a duration of 25 ps, which was refined for an additional 100 ps. The epsilon value for the Hestenes-Stiefel method of the conjugate gradient was set to 0.001[46]. The resulting structure was further optimized with a water dielectric constant of 78.39 and an effective radius of 1.3 using the semi-empirical PM7 method within a supercontinuum environment[47]. The initial charge of the copper (+1) was defined based on the state calculation. Baker's Eigen method was used in the configuration interaction calculation[48] providing analysis of the quantum state and number. Energy partitioning was performed to determine the system's energy terms, and the total energy was derived by summing the electronic and nuclear term contributions. Additionally, during each transition state refinement through single-point energy calculations, a normal density matrix comprising atomic orbitals s, p_x, p_y, and p_z was used to model interatomic interactions.

RESULTS AND DISCUSSION
Synthesis and characterization of Cu/TiO$_2$
The Cu/TiO$_2$ and undoped TiO$_2$ NPs were synthesized using a solvothermal alcoholysis method [Supplementary Figure 1], where copper (II) acetate was added as a dopant with titanium (IV) isopropoxide

as the TiO_2 precursor. The crystal structure of Cu/TiO_2 NPs was characterized using powder XRD [Supplementary Figure 2A]. Cu-doping did not change the anatase crystal structure. Both Cu/TiO_2 and undoped TiO_2 NPs were anatase phase (JCPDS-21-1272) and no reflections corresponding to metallic Cu or its oxides (CuO or Cu_2O) were observed. Additionally, no significant shifts were observed in peak positions of the Cu/TiO_2 sample compared to undoped TiO_2. The morphologies of Cu/TiO_2 and undoped TiO_2 NPs were elucidated using TEM [Supplementary Figure 2B and C] and HAADF [Figure 1A] STEM. There was no significant difference between both the shape and sizes of Cu/TiO_2 (19 ± 4 nm) and undoped TiO_2 NPs (18 ± 3 nm), although the polydispersity index describing the NP size distribution increased from 0.038 to 0.055 with the introduction of copper dopant [Supplementary Figure 3].

The elemental composition of Cu/TiO_2 determined using energy-dispersive X-ray (EDX) spectroscopy showed that the atomic fraction of Cu is 0.16% in the crystal, ~200 times lower than that of Ti atoms (~32%) in the NP lattice [Supplementary Table 1]. EDX elemental mapping [Figure 1A, Supplementary Figure 2D and E] shows a uniform distribution of Cu atoms within the TiO_2 crystal structure, indicating that the atomic ratio of Cu:Ti was 1:200 on both the surface and in the bulk of each Cu/TiO_2 NP. The chemical compositions and states of the Cu/TiO_2 and undoped TiO_2 NP surfaces were characterized via X-ray photoelectron spectroscopy (XPS). The high-resolution spectrum for Ti 2p on undoped TiO_2 NPs [Figure 1B] primarily features two peaks corresponding to the Ti^{4+} oxidation state: Ti^{4+} $2p_{3/2}$ and Ti^{4+} $2p_{1/2}$ at binding energies of 458.6 and 464.3 eV, respectively. The Cu-doping led to a small shift (~0.3 eV) of the Ti^{4+} $2p_{3/2}$ and Ti^{4+} $2p_{1/2}$ binding energies to 458.9 and 464.6 eV, respectively, in the Cu/TiO_2 sample [Figure 1C]. The increase in binding energy is attributed to the incorporation of Cu^{2+} ions into the TiO_2 lattice, indicating the formation of Ti-O-Cu linkages[18,49-51]. The Ti^{3+} $2p_{3/2}$ and Ti^{3+} $2p_{1/2}$ peaks were observed at 457.2 and 462.4 eV, respectively, and a ~36% increase in Ti^{3+} peak area was observed in Cu/TiO_2 relative to that of undoped TiO_2 NPs. Previous research has established that oxygen vacancies (OVs) reside exclusively in the subsurface bulk[52]. The extra electrons associated with the OVs are transferred to an empty 3d orbital of adjacent Ti^{4+} atoms in the TiO_2 lattice forming Ti^{3+} sites[53,54]. Supplementary Figure 4A and B shows the O 1s spectra of doped and undoped TiO_2 that were deconvoluted into two peaks at ~530 and 531 eV, which were respectively assigned to the characteristic peaks of (1) the subsurface lattice oxygen and (2) the surface oxygen including the surface lattice oxygen and the chemisorbed oxygen[51,55]. A 37.4% increase in surface oxygen was observed for Cu/TiO_2 relative to undoped TiO_2 NPs which is attributed to more dissolved oxygen (DO) chemisorbed onto Cu/TiO_2 surfaces because of the high affinity of the surface Cu^{2+} towards oxygen molecules[51]. This was further validated using computational simulation of the adsorption of DO in water on the Cu/TiO_2 surfaces [Supplementary Figure 5], concurring with previous research[56]. Further, Cu-doping increased the hydrophilicity of the NP surface [Supplementary Figure 6], where Cu also serves as the adsorption site of water based on computational simulation [Supplementary Figure 7], which is important for forming •OH on the NP surfaces.

The electronic structure of Cu/TiO_2

Broad light absorption and efficient charge separation are critical for enhanced photocatalytic activity[57,58]. To estimate the optical band gap of Cu/TiO_2, UV-Visible diffuse reflectance spectroscopy was employed to measure its light absorbance. As shown in Figure 1D, the Cu/TiO_2 NPs exhibited a noticeable redshift in absorption relative to undoped TiO_2, attributed to the $2E_g \rightarrow 2T_{2g}$ transitions from lattice O to the doped Cu atoms, which lowered the optical band gap of the material. In addition, a broad absorption hump between 450 and 650 nm was observed, which is attributed to OVs near the Cu atoms[57]. These OVs slightly distort the octahedral symmetry of the surrounding environment and facilitate d–d transitions within the Cu atoms[59]. Accordingly, the optical band gap of Cu/TiO_2 was estimated to be 2.9 eV using Tauc plots [Supplementary Figure 8]. In contrast, the undoped TiO_2 NPs do not significantly absorb light above 400 nm due to an estimated band gap of 3.20 eV. Therefore, the Cu/TiO_2 powder exhibits a slight yellow
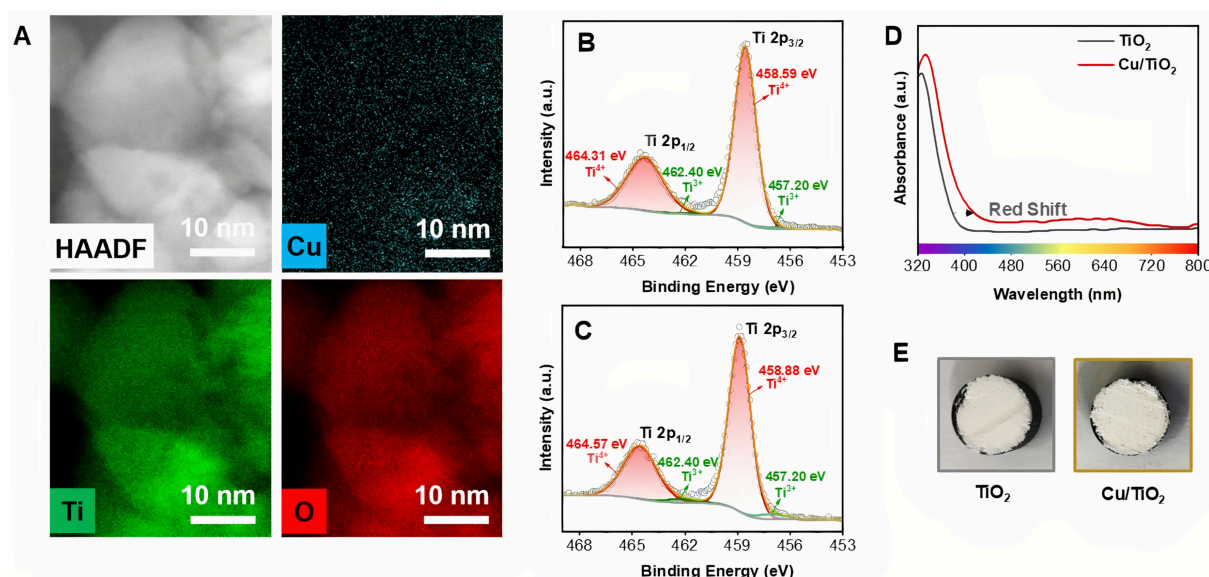
Figure 1. Characterization of Cu/TiO$_2$ nanocatalyst (Cu/TiO$_2$). (A) The HAADF scanning transmission electron microscopic image and elemental maps of Cu/TiO$_2$ NPs; High-resolution XPS spectra: the Ti 2p region for (B) TiO$_2$ and (C) Cu/TiO$_2$; (D) The UV-Vis DRS of TiO$_2$ and Cu/TiO$_2$; (E) Photographs of TiO$_2$ and Cu/TiO$_2$ powders. HAADF: High-angle annular dark-field; NPs: nanoparticles; XPS: X-ray photoelectron spectra; UV-Vis DRS: ultraviolet-visible diffuse reflectance spectra.

coloration, whereas the undoped TiO$_2$ remains white [Figure 1E].

Further, the E$_{FB}$ of Cu/TiO$_2$ was determined with Mott-Schottky analysis at 1 kHz. Accordingly, the CB potential (E$_{CB}$) in energy diagrams for Cu/TiO$_2$ was calculated as -0.45 V, below the E$_{CB}$ of the undoped TiO$_2$ (E$_{CB}$ = -0.61 V), as shown in Figure 2A. The positive slopes of both plots indicate that both NPs possess n-type semiconductor characteristics, as illustrated in Figure 2B. Based on the E$_{CB}$ and E$_{VB}$ of Cu/TiO$_2$, the photoelectrons have sufficient energy to reduce oxygen to form O$_2{}^{•-}$ and the holes are sufficiently energetic to oxidize water to produce $^{•}$OH[60].

The photoelectric properties of Cu/TiO$_2$

In addition to broad light absorption, efficient photocatalysts require production of abundant active charge carriers with long lifetimes, allowing for their diffusion from the bulk to the surface where they can react with oxygen or water to produce ROS. To evaluate the photoconversion efficiency, we measured the photocurrent response under visible LED light irradiation (400-800 nm). As shown in Figure 2C, the steady-state photocurrent density of Cu/TiO$_2$ (~3 μA·cm^{-2}) was 15 times greater than that of undoped TiO$_2$ (~0.2 μA·cm^{-2}). The increased photocurrent density in the NPs suggests a larger number of photoelectrons produced than undoped TiO$_2$, which were attributed to increased light absorption in that wavelength range and improved charge separation due to Cu-doping, where Cu^{2+} within the lattice serves as an electron acceptor to prevent recombination.

The CTR of Cu/TiO$_2$ is also critical as it affects the charge transport rate. Herein, the CTR of Cu-doped and the undoped TiO$_2$ with and without visible light irradiation was determined by EIS. As the diameter of the semi-circle in a Nyquist plot [Figure 2D] is proportional to the CTR of a sample, the result provides insights into the charge migration process. Under the same testing conditions, the CTR for Cu/TiO$_2$ NPs is much smaller than that of the undoped TiO$_2$ NPs, suggesting efficient electron transmission in the Cu/TiO$_2$ due to Cu-doping. Notably, light irradiation enhanced the electron transport in both the doped and the undoped
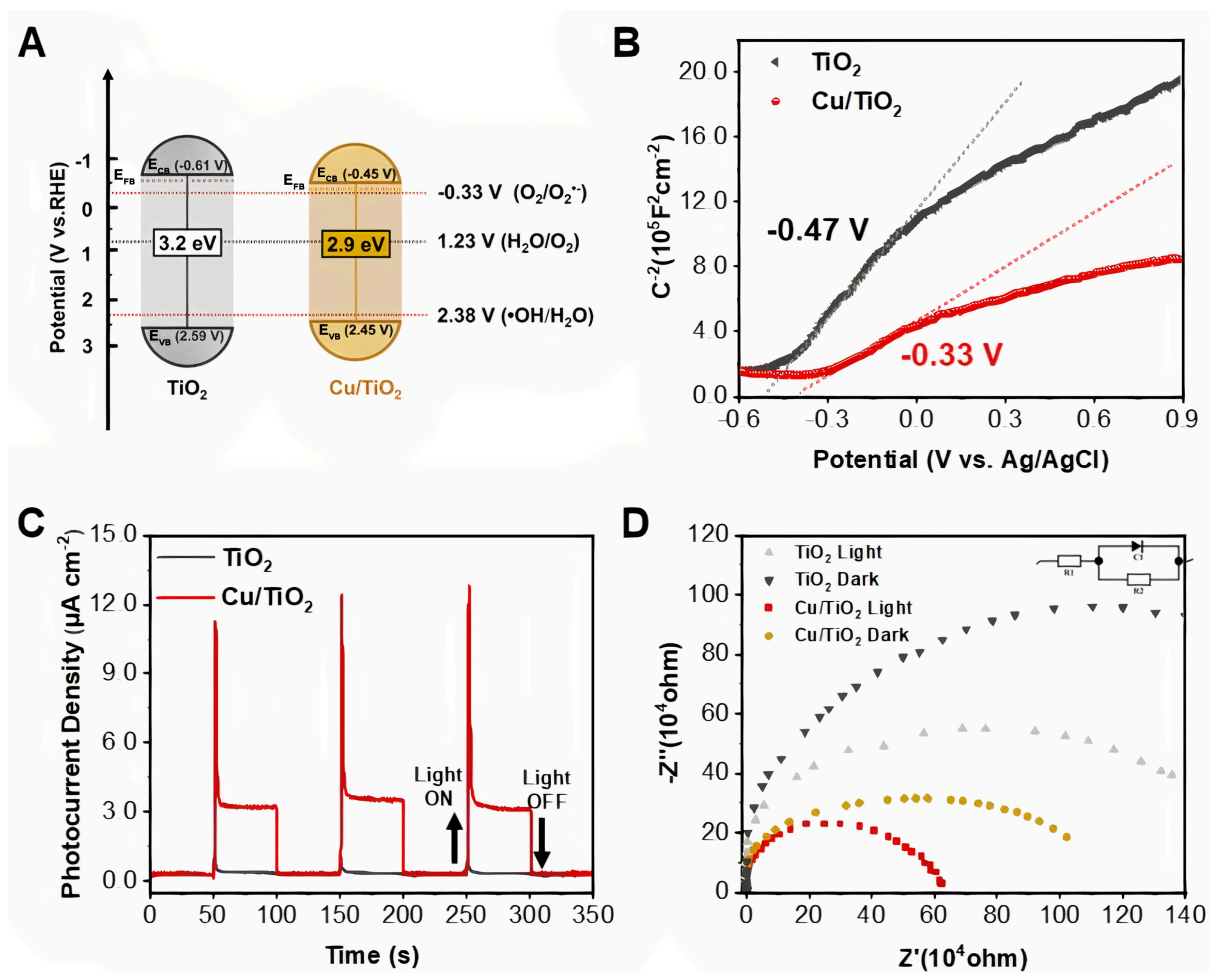
Figure 2. (A) Schematic illustration of the electronic band structure; (B) The Mott–Schottky analysis of TiO_2 and Cu/TiO_2; (C) The photocurrent and (D) the electrochemical impedance spectra for TiO_2 and Cu/TiO_2. The inset shows the equivalent circuit, consisting of R1 (solution resistance), C1 (constant phase element), and R2 (CTR). CTR: Charge transfer resistance.

TiO_2, evidenced by the smaller semi-circle diameters under irradiation than in the dark[61].

When comparing the photoelectronic properties of our Cu/TiO_2 with similar nanomaterials reported in the literature [Supplementary Table 2], we observe a complex interplay among dopants (types and concentrations), structural characteristics (e.g., solid NPs, mesoporous materials, and thin films), and photoelectrical properties (e.g., bandgap, photocurrent density, and CTR). Further efforts are needed to elucidate these relationships to optimize the design and fabrication of Cu/TiO_2 for improved performance in various applications.

Identification of ROS generated on Cu/TiO_2 surfaces

To identify the active centers on the Cu/TiO_2 surface and understand its working mechanisms regarding ROS generation under visible light irradiation [Figure 3A], the types of ROS generated were determined using EPR measurements with the spin trap 5,5'-dimethyl-1-pyrroline N-oxide (DMPO). Under visible light illumination, we observed signals from both the superoxide ions ($O_2^{\bullet-}$) and hydroxyl radicals ($^\bullet OH$) with typical splitting patterns of 1:2:2:1 for DMPO-$^\bullet OH$ (Figure 3B, where pure water was used as the solvent to disperse the nanocatalysts) and 1:1:1:1 for DMPO-$O_2^{\bullet-}$ (where methanol was used as the solvent) in
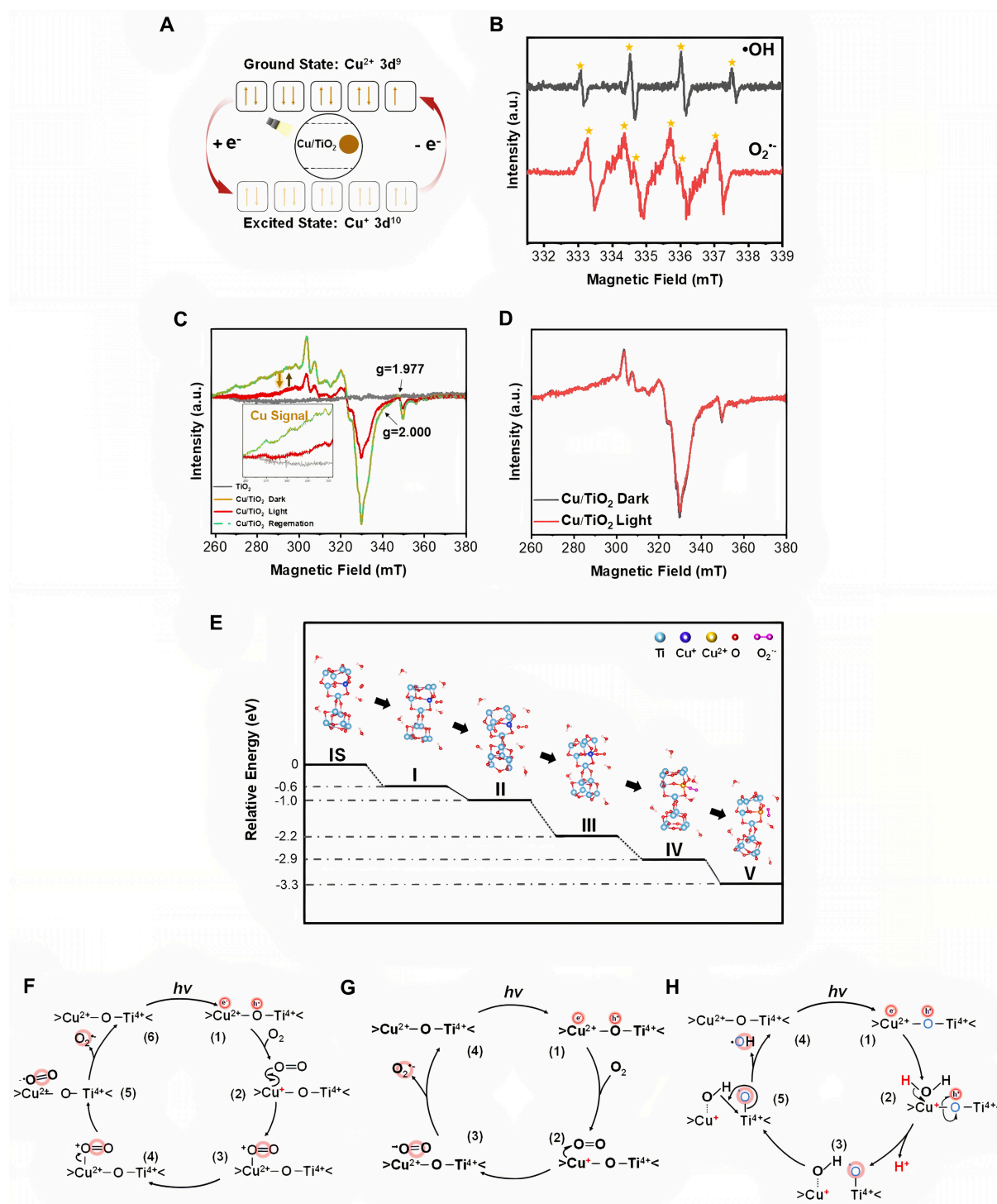
Figure 3. ROS identification and the generation mechanisms. (A) Schematic illustration of the reversible change of the shell electrons during the cycling of Cu^{2+} and Cu^+ on the surface of Cu/TiO_2 NPs; (B) The EPR spectra of radical adducts trapped by DMPO in Cu/TiO_2 under visible light irradiation, where DMPO-$^\bullet$OH formed in aqueous dispersions and DMPO-$O_2^{\bullet-}$ formed in methanol dispersions; The EPR spectra of the TiO_2 and Cu/TiO_2 (C) under nitrogen and (D) in air. Inset in (C): the characteristic hyperfine structure of the Cu signal; (E) DO adsorbed on the excited state of Cu/TiO_2 (bearing Cu^+) in water; (F) The mechanism of superoxide generation via inner sphere electron transfer, including the following steps: (1) formation of charge carriers by photon absorption, whereafter Cu^{2+} is converted to Cu^+ by trapped photoelectrons; (2) Cu^+ and DO form a new sigma bond by each donating a single electron; (3) generation of intermediate (Cu^{2+}-dioxyenyl); (4) dioxygenyl cation accepts both sigma electrons during heterolytic Cu–O bond cleavage; (5) superoxide radical ion formation; (6) superoxide radical ion diffused off of the Cu/TiO_2 surface; (G) The mechanism of superoxide

generation via outer sphere electron transfer, including the following steps: (1) formation of charge carriers by photon absorption, whereafter Cu^{2+} trapped photoelectrons; (2) photoelectrons in the Cu site react with physisorbed oxygen; (3) desorption of reduced O_2 to form superoxide ions; (4) superoxide radical diffused off the Cu/TiO_2 surface; (H) The mechanism of hydroxyl radical generation, including the following steps: (1) formation of charge carriers by photon absorption and homolytic Cu–O bond cleavage wherein h^+ accepts one electron and the other remains on O with simultaneous nucleophilic attack on Cu by water; (2) formation of Ti-O$^\bullet$ and Cu-OH; (3) proton transfer between Ti-O$^\bullet$ and Cu-OH with displacement of hydroxyl radical by nucleophilic attack of Cu-O onto Ti; (5) hydroxyl radical diffuses away from the Cu/TiO_2 surface. Note: In f, g, and h, a half arrow represents the transfer of one electron, while a full arrow represents a transfer of two electrons. ROS: Reactive oxygen species; NPs: nanoparticles; EPR: electron paramagnetic resonance; DMPO: 5,5-dimethyl-1-pyrroline N-oxide; DO: dissolved oxygen.

Cu/TiO_2[43,62]. In contrast, no detectable levels of ROS were generated by either the doped in the dark or by undoped TiO_2 under visible light irradiation [Supplementary Figure 9]. These results confirm that only the doped (not the undoped) TiO_2 can be excited by visible light to form ROS, and that the ROS formation was caused by a photoexcitation reaction rather than a secondary process in the dark.

To identify the effective wavelength range of the photons that induce the ROS generation, we detected the production of $O_2^{\bullet-}$ and $^\bullet OH$ using the selective probes XTT and coumarin, respectively, under a white light LED using four wavelength cut-off filters of ≥ 400, 420, 450, and 500 nm. As depicted in Supplementary Figure 10, using a light cut-off filter at 400 nm, the Cu/TiO_2 NPs produced a large amount of $O_2^{\bullet-}$ and $^\bullet OH$. As the cut-off wavelength increased, there was a notable decrease in the amount of ROS formed. After the wavelength exceeded 450 nm, almost no ROS generation was observed. These results show that the Cu/TiO_2 NPs can produce ROS under irradiation with visible light between 400-500 nm. Compared to undoped TiO_2, the rates of $O_2^{\bullet-}$ and $^\bullet OH$ production by Cu/TiO_2 under visible light irradiation ($\lambda \geq 400$ nm) were 7.2 and 11.2 times larger, respectively [Supplementary Table 3].

ROS formation mechanisms on Cu/TiO_2 surfaces

To investigate the $O_2^{\bullet-}$ formation via oxygen reduction on Cu/TiO_2 surface, EPR spectroscopy was used to measure the transformation of critical chemical species with unpaired electrons (including Cu^{2+}, OVs, and Ti^{3+}) with and without irradiation, and under an air or nitrogen atmosphere. Under nitrogen gas, the Cu/TiO_2 NPs showed an EPR signal of Cu^{2+} with the characteristic hyperfine structure around 260-300 mT in the dark [Figure 3C][25]. Importantly, the signal revealed the presence of only one Cu^{2+} species, characterized by the resonance parameter $g_{//} = 2.33$ [Figure 3C and Supplementary Figure 11], which was attributed to discrete Cu^{2+} occupying substitutional cation sites within the TiO_2 lattice, specifically in the Cu-O-Ti linkage[49,63]. No Cu^{2+} signals indicative of its presence in CuO clusters ($g_{//} = 2.24$) were observed, in line with the EDX-based Cu images with the size of ~172 ± 8 pm [Supplementary Figure 2D and E], which is similar to those results published recently[64,65].

Strikingly, the signal intensity of Cu^{2+} decreased significantly after 10 min of irradiation, indicating the reduction of Cu^{2+} to Cu^+ by photoelectrons and consequent loss of EPR signal. However, exposure to air restored the EPR signal intensity of Cu^{2+}, which was attributed to the re-oxidation of surface Cu^+ by oxygen, showing the reversible valence change of Cu ($Cu^{2+} + e^- \rightleftharpoons Cu^+$) on the surface of Cu/TiO_2 NPs. In contrast, the EPR signal intensity of Cu^{2+} did not decrease in air during irradiation [Figure 3D], suggesting that the surface Cu^+ formed by photoelectron reduction of Cu^{2+} was instantaneously oxidized by oxygen. Because the photoreduction is the rate determining step (i.e., photoreduction is the slower step than oxidation), the Cu^{2+} EPR signal remained constant. These results revealed that the surface Cu atoms are the active centers for oxygen reduction and formation of $O_2^{\bullet-}$. As a control, the reference material, undoped TiO_2, did not produce any EPR signal because it is diamagnetic and has no unpaired electrons.

Notably, the results in Figure 3C do not support the hypothesis that $O_2^{\bullet-}$ formation was mediated by electrons donated from OVs or Ti^{3+}, which might participate in other previous work[66,67]. The EPR signal for Ti^{3+} (g = 1.977) barely changed both during irradiation and in the dark under nitrogen, or after regeneration in air, indicating that Ti^{3+} did not contribute significantly to oxygen reduction[68]. The OV signal intensity (g = 2.000) decreased slightly during irradiation under nitrogen relative to that in the dark or after air exposure, attributable to the reaction of OVs with photoelectrons[69]. Admittedly, OVs and Ti^{3+} are important defects that can modify the band gaps and improve the catalytic activities of many metal oxides; however, their surface concentrations on Cu/TiO_2 may be too low relative to that of Cu^+ to serve as the active centers in the Cu/TiO_2 catalyst.

Based on the computational simulation of the oxygen adsorption process, the oxygen dissolved in water can adsorb onto Cu/TiO_2 that was either in the ground state (in the dark, physisorption, Supplementary Figure 5) bearing Cu^{2+} or in the excited state (during visible light irradiation, physisorption followed by chemisorption, Figure 3E) bearing Cu^+ on the surface. Both reaction mechanisms, i.e., outer-sphere [Figure 3F] and inner-sphere [Figure 3G] electron transfer, may contribute to $O_2^{\bullet-}$ formation. The outer-sphere electron transfer applies to physisorbed oxygen on the Cu/TiO_2 surface (State III in Figure 3E), whereas the inner-sphere electron transfer applies to chemisorbed oxygen (State IV in Figure 3E). Importantly, in both mechanisms, (1) Cu^{2+} traps photoelectrons to form Cu^+, which suppresses charge recombination so that the holes can migrate to Cu/TiO_2 surface to participate in surface reactions to produce $^{\bullet}OH$; and (2) Cu^+ donates the electron to the adsorbed oxygen to form $O_2^{\bullet-}$. As a result, Cu serves as an electron storage cell that collects the photoelectrons when generated by the anatase and releases them when the electron acceptors, such as DO, are adsorbed nearby, thus maintaining a high concentration of effective charge carriers on the surface of Cu/TiO_2 for interfacial redox reactions.

The $^{\bullet}OH$ generation mechanism on the Cu/TiO_2 surface is illustrated in Figure 3H. Herein, $^{\bullet}OH$ was formed due to oxidation of the lattice oxygen, and not the adsorbed water molecule, on the surface by photogenerated holes, which will leave an OV that will be filled by an adsorbed water molecule on Cu, which has been established by abundant experimental evidence and simulations[70-74]. Relative to the bridging Ti-O-Ti structure, bridging Cu-O-Ti facilitates oxidation of the lattice oxygen, because Cu is more electron-rich than Ti and can stabilize holes in the transition state. Notably, our computational simulation indicated that when water molecules interacted with Cu atoms on Cu/TiO_2 surface, hydroxide anions produced from water ionization were preferentially adsorbed to the Cu atoms on Cu/TiO_2 surfaces in both excited [Supplementary Figure 7A] or ground [Supplementary Figure 7B] states.

Cu/TiO_2 for water treatment

To test the efficacy of Cu/TiO_2 for water treatment, we measured their waterborne dye degradation, bactericidal, and biofilm disruption ability, because organic molecules, planktonic microbes, and biofilms represent some of the most common water quality challenges. The experimental set-up for dye degradation is shown in Figure 4A. In the photodegradation experiment, RhB, an established model organic pollutant in water treatment research, was used to test the photocatalytic efficiency of Cu/TiO_2 [Figure 4B][75,76]. The initial concentration was 5 mg/L, which is ~36 times higher than the maximum acceptable concentration for RhB (140 µg/L) in water[77]. For comparison, RhB degradation using undoped TiO_2 was evaluated in parallel as a reference. The results showed a ~4-times increase in the photodegradation rate by the doped relative to undoped TiO_2 [Figure 4B and C, Supplementary Figure 12]. The RhB photodegradation by undoped TiO_2, despite its low rate, was attributed to the dye-photosensitized oxidation mechanism[76]. The pH of the samples significantly influenced the rate of RhB degradation [Supplementary Figure 13], with faster degradation observed under acidic conditions compared to basic solutions. This behavior is attributed to variations in surface charge at different pH levels. Under acidic conditions, RhB is protonated and
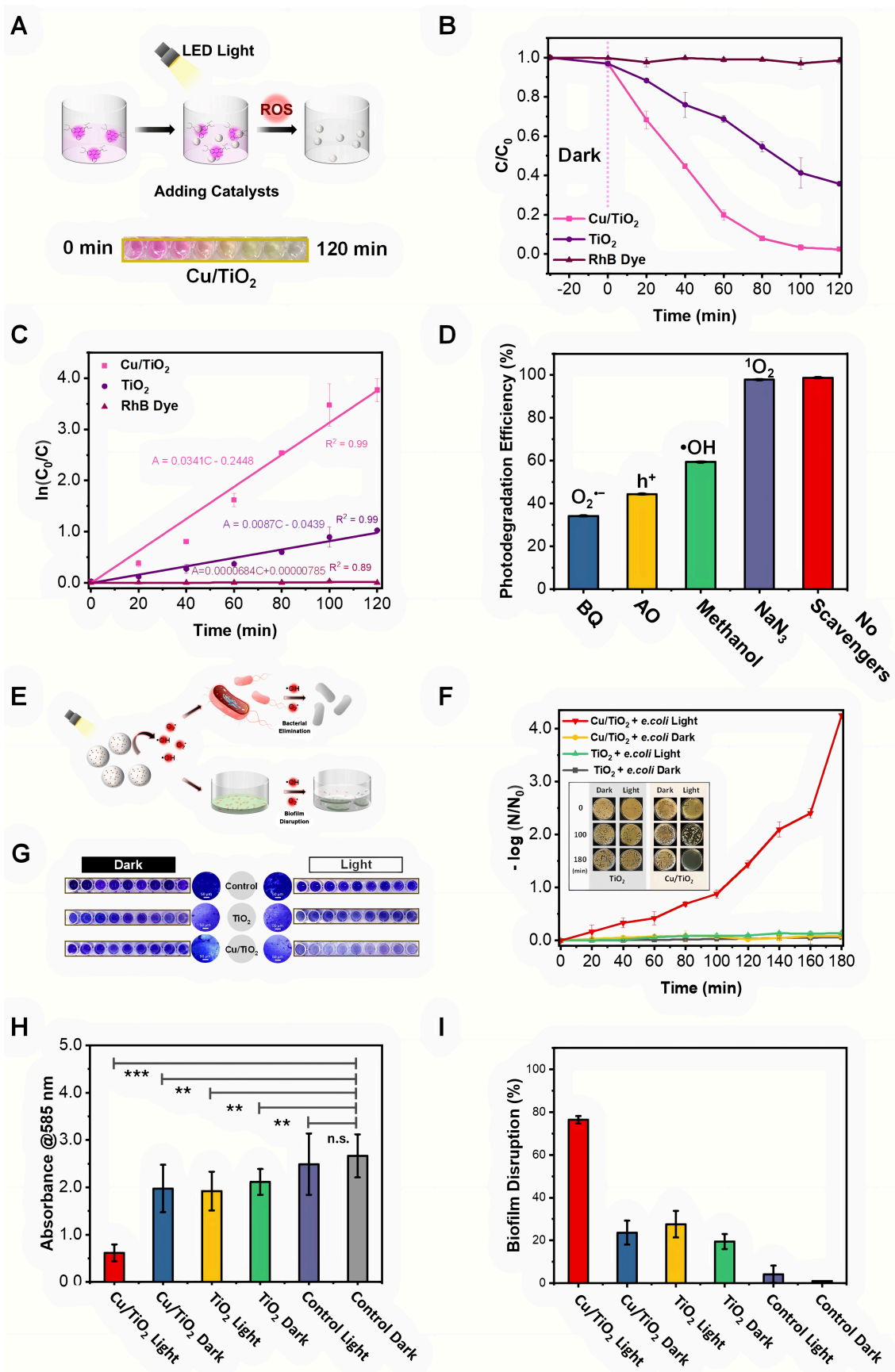
Figure 4. Evaluation of Cu/TiO$_2$ for the removal of common water pollutants: organic dye, bacteria, and biofilm. (A) Scheme of photocatalytic degradation of RhB dye using Cu/TiO$_2$; (B) The degradation kinetics of RhB using TiO$_2$ and Cu/TiO$_2$; (C) The fitted first-order degradation kinetics of RhB by Cu/TiO$_2$ under visible light irradiation; (D) The effect of various scavengers on the RhB degradation over 3 h; (E) Scheme of photocatalytic destruction of planktonic *E. coli* by Cu/TiO$_2$ NPs under visible light irradiation; (F) *E. coli* inactivation rates of TiO$_2$ and Cu/TiO$_2$ NPs with and without visible light irradiation. Inset: Photographs of bacterial colonies of *E. coli* treated with TiO$_2$ and Cu/TiO$_2$ NPs with and without visible light irradiation over time; (G) The optical and microscope images of the biofilm in the microplate wells after treatment with TiO$_2$ and Cu/TiO$_2$ (H) The CV assay showing the remaining biofilm after treatment with TiO$_2$ and Cu/TiO$_2$ under 180-min visible light irradiation or in the dark; (I) The biofilm disruption efficacy of TiO$_2$ and Cu/TiO$_2$ (scale bars represent standard deviation of nine replicates ($n = 9$) (mean ± SD); n.s > 0.05; $^{**}P > 0.05$; $^{***}P > 0.001$). RhB: Rhodamine B; NPs: nanoparticles; CV: crystal violet.

uncharged, allowing it to be readily adsorbed onto the protonated Cu/TiO$_2$ NPs, facilitating degradation. Conversely, under highly basic conditions (e.g., pH 11), both RhB and the Cu/TiO$_2$ NPs carry negative charge, leading to electrostatic repulsion and hindering adsorption and subsequent degradation [Supplementary Figure 14].

The Cu/TiO$_2$ demonstrated excellent reusability because of its structural stability and consistent reactivity, which are valuable from an application and sustainability perspective. As evidenced in Supplementary Figure 15A, after five use cycles including irradiation, filtration, washing, and drying, the photocatalytic activity of Cu/TiO$_2$ remained constant, with a ~4% decrease that was attributed to the loss of a small amount of Cu/TiO$_2$ during rinsing. The XRD and TEM analysis of Cu/TiO$_2$ before and after the five cycles revealed no difference in its morphology or crystal structure [Supplementary Figure 15B and C].

To identify the ROS generated by Cu/TiO$_2$ during RhB degradation, selective ROS scavengers were introduced into the reaction system, including methanol, AO, BQ, and sodium azide (NaN$_3$) that trap $^•$OH, photon-induced holes, O$_2^{•-}$, and singlet oxygen (^{1}O$_2$), respectively[43,44,78]. RhB degradation was inhibited by BQ (60%), AO (55%), and methanol (40%), but not by NaN$_3$ [Figure 4D and Supplementary Figure 16], indicating that the ROS responsible for RhB degradation included $^•$OH, photon-induced holes, and O$_2^{•-}$, but not ^{1}O$_2$. As the precursor of $^•$OH, the holes migrating to Cu/TiO$_2$ surface can directly oxidize adsorbed RhB molecules[79]. Simultaneously, the charge carriers could produce ROS (O$_2^{•-}$ and $^•$OH) that diffused into the bulk solution to degrade free RhB. The results of the scavenging experiments were consistent with the ROS identification using EPR and ROS probes in Figure 3B and Supplementary Figure 10.

To understand the function of DO in the photocatalytic process, we compared the ROS generation and RhB photodegradation in the presence and absence of DO. Supplementary Figure 17 shows that the production of both O$_2^{•-}$ and $^•$OH were significantly inhibited when the DO was removed by nitrogen sparging, and accordingly RhB degradation was inhibited. As the precursor of O$_2^{•-}$, DO is reduced by Cu$^+$ [Figure 3F and G], which explains the inhibition of the O$_2^{•-}$ production in the absence of DO in water. Moreover, without DO as the final electron acceptor, the accumulation of Cu$^+$ on Cu/TiO$_2$ surface will scavenge the holes generated by Cu/TiO$_2$, which leads to a decrease in $^•$OH production. Taken together, DO not only serve as the precursor of O$_2^{•-}$, but also facilitates the catalytic cycling of Cu^{2+} and Cu$^+$, thus promoting $^•$OH production.

Finally, the photocatalytic bactericidal efficacy of Cu/TiO$_2$ was evaluated. Herein, *E. coli* was used as a model organism because of its wide presence in contaminated water [Figure 4E]. The bacteria cells that survived after treatment by either the doped or undoped TiO$_2$ NPs for 3 h were plated onto Tryptic Soy (TS) agar for counting. To test the toxicity of Cu/TiO$_2$, we first evaluated the bactericidal activity in darkness. The results show negligible antibacterial activity of Cu/TiO$_2$ in the dark, similar to undoped TiO$_2$ NPs. However, under visible light irradiation, Cu/TiO$_2$ exhibited excellent disinfection properties, reducing the number of bacteria

over time and up to 4.3 log values after 3 h [Figure 4F and Supplementary Figure 18]. In contrast, the undoped TiO_2 NPs did not display any antibacterial activity, attributed to negligible ROS production [Supplementary Figure 9].

Encouraged by the excellent bactericidal efficacy of Cu/TiO_2, we further tested its ability to photodegrade established bacterial biofilms. Herein, "established biofilm" refers to biofilms that cannot be removed through simple washing steps, though they may not have reached maturity. Using the CV assay, Figure 4G-I illustrates the superior biofilm disruption (~76%) of Cu/TiO_2 under visible light irradiation over 3 h relative to either irradiated undoped TiO_2 NPs (~20%) or Cu/TiO_2 in the dark (~20%). More biofilm was disrupted (76%, 85%, and 92%) with extended time from 3, 6, and 9 h, respectively, evidenced by both the CV assay and micrographs of the biofilms grown on glass slides. After 9 h of Cu/TiO_2 treatment, only a few dispersed bacteria were observed, with no discernible biofilm structure remaining [Supplementary Figure 19].

Notably, this result is significant in water treatment research and the environmental sciences. Biofilms are often implicated in sterilization failure and infections because they exhibit complex phenotypic traits and the bacterial communities within biofilms are well-protected within a dense matrix of extracellular polymeric substances (EPSs). This makes them highly resistant to conventional antibiotic or disinfectant treatment, which significantly increases bacterial resistance to environmental stresses. Nevertheless, the large number of potent ROS generated by Cu/TiO_2 completely degraded the EPS and deactivated all resident bacteria cells protected by the EPS within the biofilm. Compared to other Cu-doped or composite TiO_2 materials for water treatment [Supplementary Table 4], the Cu/TiO_2 reported in this study exhibited not only high dye degradation efficiency but also faster bacteria elimination and biofilm eradication under visible light irradiation.

CONCLUSIONS

ROS play a primary role in advanced oxidation/reduction processes for water treatment. Cu/TiO_2 NPs efficiently produce ROS under visible-light irradiation. This work documents an atomistic understanding of the mechanisms of ROS production by Cu/TiO_2. On the one hand, the isolated Cu atoms in anatase modify the electronic, photoelectric, and surface properties of TiO_2, which make the anatase an excellent light absorber and photocurrent generator by narrowing the bandgap that allows for visible light excitation, improving charge separation and migration, and facilitating surface adsorption of DO; on the other hand, the discrete Cu atoms on the surface of anatase serve as the active sites for reduction of DO to form $O_2^{\cdot-}$ and for oxidation of lattice oxygen to form $^{\cdot}OH$. The high activity in ROS production is due to the cooperative interactions between Cu and the anatase. The potent ROS generated enabled efficient removal of organic dye, planktonic bacteria, and established biofilms, and are thus promising for off-grid water treatment applications, e.g., for fabricating point-of-use devices for remote communities that lack energy infrastructure or for treating polycyclic aromatic hydrocarbons in oil sands tailing ponds while remaining environmentally friendly and cost-effective[80].

DECLARATIONS

Authors' contributions
Conceptualization, investigation, methodology, data processing, and writing - original draft: Yu, N.
Investigation, data processing, and visualization: Nganou, C.
Methodology and writing - original draft: Yang, D.
Investigation, visualization, writing - review and editing: Carrier, A.
Writing - review and editing, funding acquisition: Oakes, K.

Conceptualization, supervision, work administration, and writing - review and editing: Dasog, M.
Conceptualization, supervision, work administration, writing - original draft, writing - review and editing, funding acquisition: Zhang, X.

Availability of data and materials
The data and materials generated and analyzed during this study are available from the corresponding author upon reasonable request.

Financial support and sponsorship

Conflicts of interest
All authors declared that there are no conflicts of interest.

Ethics approval and consent to participate
Not applicable.

Consent for publication
Not applicable.

Copyright

REFERENCES

1. Fujishima, A.; Honda, K. Electrochemical photolysis of water at a semiconductor electrode. *Nature* **1972**, *238*, 37-8. DOI
2. Zhang, H.; Chen, D.; Lv, X.; Wang, Y.; Chang, H.; Li, J. Energy-efficient photodegradation of azo dyes with TiO_2 nanoparticles based on photoisomerization and alternate UV-visible light. *Environ. Sci. Technol.* **2010**, *44*, 1107-11. DOI
3. Hashimoto, K.; Hiramoto, M.; Sakata, T. Temperature-independent electron-transfer: Rhodamine B/oxide semiconductor dye-sensitization system. *J. Phys. Chem.* **1988**, *92*, 4272-4. DOI
4. Basavarajappa, P. S.; Patil, S. B.; Ganganagappa, N.; Reddy, K. R.; Raghu, A. V.; Reddy, C. V. Recent progress in metal-doped TiO_2, non-metal doped/codoped TiO_2 and TiO_2 nanostructured hybrids for enhanced photocatalysis. *Int. J. Hydrogen. Energy.* **2020**, *45*, 7764-78. DOI
5. Paola, A. D.; Ikeda, S.; Marcì, G.; Ohtani, B.; Palmisano, L. Transition metal doped TiO_2: physical properties and photocatalytic behaviour. *Int. J. Photoenergy.* **2001**, *3*, 171-6. DOI
6. Wang, B.; Shen, S.; Mao, S. S. Black TiO_2 for solar hydrogen conversion. *J. Materiomics.* **2017**, *3*, 96-111. DOI
7. Zhang, K.; Park, J. H. Surface localization of defects in black TiO_2: enhancing photoactivity or reactivity. *J. Phys. Chem. Lett.* **2017**, *8*, 199-207. DOI PubMed
8. Erdural, B.; Bolukbasi, U.; Karakas, G. Photocatalytic antibacterial activity of TiO_2–SiO_2 thin films: the effect of composition on cell adhesion and antibacterial activity. *J. Photochem. Photobiol. A. Chem.* **2014**, *283*, 29-37. DOI
9. Ya, J.; Yang, N.; Hu, F.; Liu, Z.; E, L. Preparation and activity evaluation of TiO_2/Cu-TiO_2 composite catalysts. *J. Sol. Gel. Sci. Technol.* **2015**, *73*, 322-31. DOI
10. Chen, F.; Zhao, J.; Hidaka, H. Highly selective deethylation of rhodamine B: adsorption and photooxidation pathways of the dye on the TiO_2/SiO_2 composite photocatalyst. *Int. J. Photoenergy.* **2003**, *5*, 209-17. DOI
11. Liu, Z.; Sun, L.; Zhang, Q.; Teng, Z.; Sun, H.; Su, C. TiO_2-supported single-atom catalysts: synthesis, structure, and application. *Chem. Res. Chin. Univ.* **2022**, *38*, 1123-38. DOI
12. Janisch, R.; Gopal, P.; Spaldin, N. A. Transition metal-doped TiO_2 and ZnO - present status of the field. *J. Phys. Condens. Matter.* **2005**, *17*, R657-89. DOI

13.   Song, H.; Li, C.; Lou, Z.; Ye, Z.; Zhu, L. Effective formation of oxygen vacancies in black TiO_2 nanostructures with efficient solar-driven water splitting. *ACS. Sustainable. Chem. Eng.* **2017**, *5*, 8982-7. DOI

14.   Hejazi, S.; Killian, M. S.; Mazare, A.; Mohajernia, S. Single-atom-based catalysts for photocatalytic water splitting on TiO_2 nanostructures. *Catalysts* **2022**, *12*, 905. DOI

15.   Tomboc, G. M.; Kim, T.; Jung, S.; Yoon, H. J.; Lee, K. Modulating the local coordination environment of single-atom catalysts for enhanced catalytic performance in hydrogen/oxygen evolution reaction. *Small* **2022**, *18*, e2105680. DOI

16.   Lee, B. H.; Park, S.; Kim, M.; et al. Reversible and cooperative photoactivation of single-atom Cu/TiO_2 photocatalysts. *Nat. Mater.* **2019**, *18*, 620-6. DOI

17.   Wang, H.; Qi, H.; Sun, X.; et al. High quantum efficiency of hydrogen production from methanol aqueous solution with $PtCu-TiO_2$ photocatalysts. *Nat. Mater.* **2023**, *22*, 619-26. DOI

18.   Fang, Y.; Zhang, Q.; Zhang, H.; et al. Dual activation of molecular oxygen and surface lattice oxygen in single atom Cu_1/TiO_2 catalyst for CO oxidation. *Angew. Chem. Int. Ed. Engl.* **2022**, *61*, e202212273. DOI

19.   Iyemperumal, S. K.; Pham, T. D.; Bauer, J.; Deskins, N. A. Quantifying support interactions and reactivity trends of single metal atom catalysts over TiO_2. *J. Phys. Chem. C* **2018**, *122*, 25274-89. DOI

20.   Qi, R.; Zhu, B.; Han, Z.; Gao, Y. High-throughput screening of stable single-atom catalysts in CO_2 reduction reactions. *ACS. Catal.* **2022**, *12*, 8269-78. DOI

21.   De, S.; Dokania, A.; Ramirez, A.; Gascon, J. Advances in the design of heterogeneous catalysts and thermocatalytic processes for CO_2 utilization. *ACS. Catal.* **2020**, *10*, 14147-85. DOI

22.   Hu, G.; Wu, Z.; Jiang, D. First principles insight into H_2 activation and hydride species on TiO_2 surfaces. *J. Phys. Chem. C* **2018**, *122*, 20323-8. DOI

23.   Liu, P.; Zhao, Y.; Qin, R.; et al. Photochemical route for synthesizing atomically dispersed palladium catalysts. *Science* **2016**, *352*, 797-801. DOI

24.   Hu, J.; Kim, E. M.; Janik, M. J.; Alexopoulos, K. Hydrogen activation and spillover on anatase TiO_2-supported Ag single-atom catalysts. *J. Phys. Chem. C* **2022**, *126*, 7482-91. DOI

25.   Li, D.; Zhao, Y.; Miao, Y.; et al. Accelerating electron-transfer dynamics by TiO_2-immobilized reversible single-atom copper for enhanced artificial photosynthesis of urea. *Adv. Mater.* **2022**, *34*, e2207793. DOI

26.   Guo, Y.; Huang, Y.; Zeng, B.; et al. Photo-thermo semi-hydrogenation of acetylene on Pd_1/TiO_2 single-atom catalyst. *Nat. Commun.* **2022**, *13*, 2648. DOI PubMed PMC

27.   Kim, S. S.; Lee, H. H.; Hong, S. C. The effect of the morphological characteristics of TiO_2 supports on the reverse water–gas shift reaction over Pt/TiO_2 catalysts. *Appl. Catal. B. Environ.* **2012**, *119-20*, 100-8. DOI

28.   Chen, L.; Unocic, R. R.; Hoffman, A. S.; et al. Unlocking the catalytic potential of TiO_2-supported Pt single atoms for the reverse water-gas shift reaction by altering their chemical environment. *JACS. Au.* **2021**, *1*, 977-86. DOI PubMed PMC

29.   Nelson, N. C.; Chen, L.; Meira, D.; Kovarik, L.; Szanyi, J. In situ dispersion of palladium on TiO_2 during reverse water–gas shift reaction: formation of atomically dispersed palladium. *Angew. Chem. Int. Ed. Engl.* **2020**, *132*, 17810-6. DOI PubMed

30.   Astruc, D.; Lu, F.; Aranzaes, J. R. Nanoparticles as recyclable catalysts: the frontier between homogeneous and heterogeneous catalysis. *Angew. Chem. Int. Ed. Engl.* **2005**, *44*, 7852-72. DOI PubMed

31.   Byrne, C.; Moran, L.; Hermosilla, D.; et al. Effect of Cu doping on the anatase-to-rutile phase transition in TiO_2 photocatalysts: theory and experiments. *Appl. Catal. B. Environ.* **2019**, *246*, 266-76. DOI

32.   Cheng, C.; Fang, W. H.; Long, R.; Prezhdo, O. V. Water splitting with a single-atom Cu/TiO_2 photocatalyst: atomistic origin of high efficiency and proposed enhancement by spin selection. *JACS. Au.* **2021**, *1*, 550-9. DOI PubMed PMC

33.   Cao, Z.; Tsai, S. N.; Zuo, Y. Y. An optical method for quantitatively determining the surface free energy of micro- and nanoparticles. *Anal. Chem.* **2019**, *91*, 12819-26. DOI PubMed

34.   Chen, X.; Liu, L.; Yu, P. Y.; Mao, S. S. Increasing solar absorption for photocatalysis with black hydrogenated titanium dioxide nanocrystals. *Science* **2011**, *331*, 746-50. DOI

35.   Kim, A.; Sanchez, C.; Haye, B.; Boissière, C.; Sassoye, C.; Debecker, D. P. Mesoporous TiO_2 support materials for Ru-based CO_2 methanation catalysts. *ACS. Appl. Nano. Mater.* **2019**, *2*, 3220-30. DOI

36.   Martell, S. A.; Werner-Zwanziger, U.; Dasog, M. The influence of hydrofluoric acid etching processes on the photocatalytic hydrogen evolution reaction using mesoporous silicon nanoparticles. *Faraday. Discuss.* **2020**, *222*, 176-89. DOI PubMed

37.   Kirshenbaum, M. J.; Richter, M. H.; Dasog, M. Electrochemical water oxidation in acidic solution using titanium diboride (TiB_2) catalyst. *ChemCatChem* **2019**, *11*, 3877-81. DOI

38.   Gelderman, K.; Lee, L.; Donne, S. W. Flat-band potential of a semiconductor: using the Mott–Schottky equation. *J. Chem. Educ.* **2007**, *84*, 685. DOI

39.   Balu, S.; Chen, Y. L.; Chen, S. W.; Yang, T. C. K. Rational synthesis of $Bi_xFe_{1-x}VO_4$ heterostructures impregnated sulfur-doped g-C_3N_4: a visible-light-driven type-II heterojunction photo(electro)catalyst for efficient photodegradation of roxarsone and photoelectrochemical OER reactions. *Appl. Catal. B. Environ.* **2022**, *304*, 120852. DOI

40.   Kautek, W.; Gerischer, H. Photoelectrochemical reactions and formation of inversion layers at n-type MoS_2-, $MoSe_2$-, and WSe_2-electrodes in aprotic solvents. *Ber. Bunsenges. Phys. Chem.* **1980**, *84*, 645-53. DOI

41.   Feenstra, R. M.; Stroscio, J. A. Tunneling spectroscopy of the GaAs(110) surface. *J. Vac. Sci. Technol. B.* **1987**, *5*, 923-9. DOI

42.   Seger, B.; Tilley, S. D.; Pedersen, T.; et al. Silicon protected with atomic layer deposited TiO_2: conducting versus tunnelling through

TiO$_2$. *J. Mater. Chem. A.* **2013**, *1*, 15089. DOI

43.   Yin, M.; Li, Z.; Kou, J.; Zou, Z. Mechanism investigation of visible light-induced degradation in a heterogeneous TiO$_2$/eosin Y/ rhodamine B system. *Environ. Sci. Technol.* **2009**, *43*, 8361-6. DOI

44.   Jo, W. K.; Kim, Y. G.; Tonda, S. Hierarchical flower-like NiAl-layered double hydroxide microspheres encapsulated with black Cu-doped TiO$_2$ nanoparticles: highly efficient visible-light-driven composite photocatalysts for environmental remediation. *J. Hazard. Mater.* **2018**, *357*, 19-29. DOI PubMed

45.   Zhang, D.; Qiu, R.; Song, L.; Eric, B.; Mo, Y.; Huang, X. Role of oxygen active species in the photocatalytic degradation of phenol using polymer sensitized TiO$_2$ under visible light irradiation. *J. Hazard. Mater.* **2009**, *163*, 843-7. DOI PubMed

46.   Yuan, G.; Meng, Z.; Li, Y. A modified hestenes and stiefel conjugate gradient algorithm for large-scale nonsmooth minimizations and nonlinear equations. *J. Optim. Theory. Appl.* **2016**, *168*, 129-52. DOI

47.   Mato, J.; Guidez, E. B. Accuracy of the PM6 and PM7 methods on bare and thiolate-protected gold nanoclusters. *J. Phys. Chem. A.* **2020**, *124*, 2601-15. DOI PubMed

48.   Baker, J. An algorithm for the location of transition states. *J. Comput. Chem.* **1986**, *7*, 385-95. DOI

49.   Li, G.; Dimitrijevic, N. M.; Chen, L.; Rajh, T.; Gray, K. A. Role of surface/interfacial Cu^{2+} sites in the photocatalytic activity of coupled CuO−TiO$_2$ nanocomposites. *J. Phys. Chem. C.* **2008**, *112*, 19040-4. DOI

50.   Moniz, S. J. A.; Tang, J. Charge transfer and photocatalytic activity in CuO/TiO$_2$ nanoparticle heterojunctions synthesised through a rapid, one-pot, microwave solvothermal route. *ChemCatChem* **2015**, *7*, 1659-67. DOI

51.   Bhattacharyya, K.; Mane, G. P.; Rane, V.; Tripathi, A. K.; Tyagi, A. K. Selective CO$_2$ photoreduction with Cu-doped TiO$_2$ photocatalyst: delineating the crucial role of Cu-oxidation state and oxygen vacancies. *J. Phys. Chem. C.* **2021**, *125*, 1793-810. DOI

52.   Setvín, M.; Aschauer, U.; Scheiber, P.; et al. Reaction of O$_2$ with subsurface oxygen vacancies on TiO$_2$ anatase (101). *Science* **2013**, *341*, 988-91. DOI

53.   Bredow, T.; Pacchioni, G. Electronic structure of an isolated oxygen vacancy at the TiO$_2$(110) surface. *Chem. Phys. Lett.* **2002**, *355*, 417-23. DOI

54.   Pacchioni, G. Oxygen vacancy: the invisible agent on oxide surfaces. *Chemphyschem* **2003**, *4*, 1041-7. DOI PubMed

55.   You, M.; Kim, T. G.; Sung, Y. Synthesis of Cu-doped TiO$_2$ nanorods with various aspect ratios and dopant concentrations. *Cryst. Growth. Des.* **2010**, *10*, 983-7. DOI

56.   Kang, L.; Wang, B.; Bing, Q.; et al. Adsorption and activation of molecular oxygen over atomic copper(I/II) site on ceria. *Nat. Commun.* **2020**, *11*, 4008. DOI PubMed PMC

57.   Colón, G.; Maicu, M.; Hidalgo, M.; Navío, J. Cu-doped TiO$_2$ systems with improved photocatalytic activity. *Appl. Catal. B. Environ.* **2006**, *67*, 41-51. DOI

58.   Takanabe, K. Photocatalytic water splitting: quantitative approaches toward photocatalyst by design. *ACS. Catal.* **2017**, *7*, 8006-22. DOI

59.   Choudhury, B.; Dey, M.; Choudhury, A. Defect generation, d-d transition, and band gap reduction in Cu-doped TiO$_2$ nanoparticles. *Int. Nano. Lett.* **2013**, *3*, 52. DOI

60.   Rengifo-Herrera, J. A.; Pulgarin, C. Why five decades of massive research on heterogeneous photocatalysis, especially on TiO$_2$, has not yet driven to water disinfection and detoxification applications? Critical review of drawbacks and challenges. *Chem. Eng. J.* **2023**, *477*, 146875. DOI

61.   Kandoth, N.; Chaudhary, S. P.; Gupta, S.; et al. Multimodal biofilm inactivation using a photocatalytic bismuth perovskite-TiO$_2$-Ru(II)polypyridyl-based multisite heterojunction. *ACS. Nano.* **2023**, *17*, 10393-406. DOI

62.   Wu, T.; Lin, T.; Zhao, J.; Hidaka, H.; Serpone, N. TiO$_2$-assisted photodegradation of dyes. 9. Photooxidation of a squarylium cyanine dye in aqueous dispersions under visible light irradiation. *Environ. Sci. Technol.* **1999**, *33*, 1379-87. DOI

63.   Amorelli, A.; Evans, J. C.; Rowlands, C. C. Electron paramagnetic resonance study of the effect of temperature upon copper-impregnated titanium dioxide powders. *J. Chem. Soc. Faraday. Trans. 1.* **1989**, *85*, 4111. DOI

64.   Shi, X.; Lin, Y.; Huang, L.; et al. Copper catalysts in semihydrogenation of acetylene: from single atoms to nanoparticles. *ACS. Catal.* **2020**, *10*, 3495-504. DOI

65.   Zhang, Y.; Zhao, J.; Wang, H.; et al. Single-atom Cu anchored catalysts for photocatalytic renewable H$_2$ production with a quantum efficiency of 56. *Nat. Commun.* **2022**, *13*, 58. DOI PubMed PMC

66.   Zhao, Y.; Zhao, Y.; Shi, R.; et al. Tuning oxygen vacancies in ultrathin TiO$_2$ nanosheets to boost photocatalytic nitrogen fixation up to 700 nm. *Adv. Mater.* **2019**, *31*, e1806482. DOI

67.   Zhao, Y.; Zhao, Y.; Waterhouse, G. I. N.; et al. Layered-double-hydroxide nanosheets as efficient visible-light-driven photocatalysts for dinitrogen fixation. *Adv. Mater.* **2017**, *29*, 1703828. DOI

68.   Dohshi, S.; Anpo, M.; Okuda, S.; Kojima, T. Effect of γ-ray Irradiation on the Wettability of TiO$_2$ single crystals. *Top. Catal.* **2005**, *35*, 327-30. DOI

69.   Pan, C.; Shen, H.; Liu, G.; et al. CuO/TiO$_2$ nanobelt with oxygen vacancies for visible-light-driven photocatalytic bacterial inactivation. *ACS. Appl. Nano. Mater.* **2022**, *5*, 10980-90. DOI

70.   Nakamura, R.; Nakato, Y. Molecular mechanism of water oxidation reaction at photo-irradiated TiO$_2$ and related metal oxide surfaces. *Solid. State. Phenom.* **2010**, *162*, 1-27. DOI

71.   Nosaka, Y.; Nosaka, A. Understanding hydroxyl radical (˙OH) generation processes in photocatalysis. *ACS. Energy. Lett.* **2016**, *1*, 356-9. DOI

72. Kim, B.; Jeong, D.; Ohta, T.; Cho, J. Nucleophilic reactivity of a copper(II)-hydroperoxo complex. *Commun. Chem.* **2019**, *2*, 187. DOI

73. Nosaka, Y.; Nosaka, A. Y. Generation and detection of reactive oxygen species in photocatalysis. *Chem. Rev.* **2017**, *117*, 11302-36. DOI PubMed

74. Nosaka, Y.; Daimon, T.; Nosaka, A. Y.; Murakami, Y. Singlet oxygen formation in photocatalytic TiO_2 aqueous suspension. *Phys. Chem. Chem. Phys.* **2004**, *6*, 2917. DOI

75. Jakimińska, A.; Pawlicki, M.; Macyk, W. Photocatalytic transformation of Rhodamine B to Rhodamine-110 - the mechanism revisited. *J. Photochem. Photobiol. A. Chem.* **2022**, *433*, 114176. DOI

76. Wu, T.; Liu, G.; Zhao, J.; Hidaka, H.; Serpone, N. Photoassisted degradation of dye pollutants. V. Self-photosensitized oxidative transformation of *Rhodamine B* under visible light irradiation in aqueous TiO_2 dispersions. *J. Phys. Chem. B.* **1998**, *102*, 5845-51. DOI

77. Skjolding, L. M.; Jørgensen, L. V.; Dyhr, K. S.; et al. Assessing the aquatic toxicity and environmental safety of tracer compounds Rhodamine B and Rhodamine WT. *Water. Res.* **2021**, *197*, 117109. DOI

78. Jańczyk, A.; Krakowska, E.; Stochel, G.; Macyk, W. Singlet oxygen photogeneration at surface modified titanium dioxide. *J. Am. Chem. Soc.* **2006**, *128*, 15574-5. DOI PubMed

79. Curry, D. E.; Andrea, K. A.; Carrier, A. J.; et al. Surface interaction of doxorubicin with anatase determines its photodegradation mechanism: insights into removal of waterborne pharmaceuticals by TiO_2 nanoparticles. *Environ. Sci. Nano.* **2018**, *5*, 1027-35. DOI

80. Loeb, S. K.; Alvarez, P. J. J.; Brame, J. A.; et al. The technology horizon for photocatalytic water treatment: sunrise or sunset? *Environ. Sci. Technol.* **2019**, *53*, 2937-47. DOI PubMed
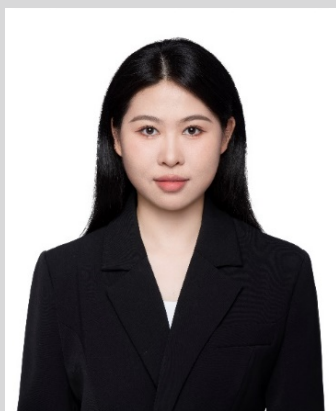
Naizhen Yu (she/her) is a research assistant at Cape Breton University, holding a Master's Degree in Chemistry from Dalhousie University. Her research focuses on developing photocatalysts for water treatment, with expertise in surface characterization techniques, reactive oxygen species (ROS) detection, and electrochemical analysis. She has extensive experience in heterogeneous catalysis, environmental remediation, and advanced oxidation processes. Her research interests include nanomaterials for sustainable applications, semiconductor design, and biosensors for water quality monitoring.

Naizhen Yu

Collins Nganou received his Ph.D. in Physics from the Institute of Optics and Atomic Physics at the Technical University Berlin, Germany. He specializes in photonics for bio-nano-systems and nanomaterials from electronic structures to transport systems. He has investigated the electronic and energy pathways of pigment-pigment and pigment-protein complexes in the cyanobacteria light-harvesting system. His current research interest focuses on developing quantum systems for energy applications and sensor technologies.

Collins Nganou

Dongchang Yang (he/him) holds a Master of Science (MSc) from the University of Waterloo and is currently a research assistant at Cape Breton University. His research focuses on advancing environmental monitoring and water treatment technologies, with expertise in analytical spectroscopy, particularly in developing surface-enhanced Raman spectroscopy (SERS) methodologies for ultrasensitive bio- and environmental detection.

Dongchang Yang

Andrew Carrier obtained his B.Sc. and Ph.D. in Chemistry from Queen's University, Canada, under the supervision of Prof. Philip Jessop. He is currently a research associate at Cape Breton University, where his research focuses on redox and free radical chemistry.

Andrew Carrier

Ken Oakes (he/him) is an Associate Professor of Biology. His research interests focus on aquatic toxicology of emerging environment pollutants, water treatment, remediation of contaminated sites, and biofouling.

He has extensive experience in investigating reactive oxygen species (ROS) generation in aquatic species exposed to industrial effluents, and the subsequent impact of ROS on steroid hormone and reproductive protein biosynthesis and oxidative stress.

Ken Oakes

Dr. Mita Dasog (she/her), Fellow of the Royal Society of Chemistry (FRSC), is an Associate Professor and Izaak Walton Killam Memorial Research Chair in the Department of Chemistry at Dalhousie University. Her research group focuses on the development of photocatalysts, electrocatalysts, and refractory plasmonic nanostructures for water treatment and clean hydrogen production. She also co-leads the Green Hydrogen Research Cluster at Dalhousie University.

Mita Dasog

Dr. Xu (Shine) Zhang (he/him) holds the Canada Research Chair (Tier II) in Healthy Environments and Communities at Cape Breton University. His fundamental research focuses on the generation, detection, exploitation, and elimination of reactive oxygen species (ROS) in environmental and biological systems. His applied research aims to exploit nanotechnology for environmental and health applications with a focus on water quality and health monitoring using SERS and electrochemical methods, and disease diagnostics and treatment with nanomedicine.

Xu Zhang